CHEMISTRY OF MATERIALS

Article

pubs.acs.org/cm

Nonstoichiometry, Structure, and Properties of $BiFeO_3$ Films

Liv R. Dedon,[†,‡] Sahar Saremi,[†] Zuhuang Chen,[†] Anoop R. Damodaran,[†] Brent A. Apgar,[†] Ran Gao,[†] and Lane W. Martin*[,†,‡]

[†]Department of Materials Science and Engineering, University of California, Berkeley, Berkeley, California 94720, United States

[‡]Materials Science Division, Lawrence Berkeley National Laboratory, Berkeley, California 94720, United States

Supporting Information

ABSTRACT: We explore the effect of growth conditions on the cation and anion chemistry, electrical leakage, conduction mechanisms, and ferroelectric and dielectric behavior of $BiFeO_3$. Although it is possible to produce single-phase, coherently strained films in all cases, small variations in the pulsed-laser deposition growth process, specifically the laser repetition rate and target composition, result in films with chemistries ranging from 10% Bi-deficiency to 4% Bi-excess and films possessing Bi gradients as large a 6% across the film thickness. Corresponding variations and gradients in the O chemistry are also observed. As a result of the varying film chemistry, marked differences in surface and domain morphology are observed wherein Bi-deficiency stabilizes atomically smooth surfaces and ordered stripe domains. Subsequent investigation of the current−voltage response reveals large differences in leakage current density arising from changes in both the overall stoichiometry and gradients. In turn, the film stoichiometry drives variations in the dominant conduction mechanism including examples of Schottky, Poole−Frenkel, and modified Poole−Frenkel emission depending on the film chemistry. Finally, slightly Bi-excess films are found to exhibit the best low-frequency ferroelectric and dielectric response while increasing Bi-deficiency worsens the low-frequency ferroelectric performance and reduces the dielectric permittivity.

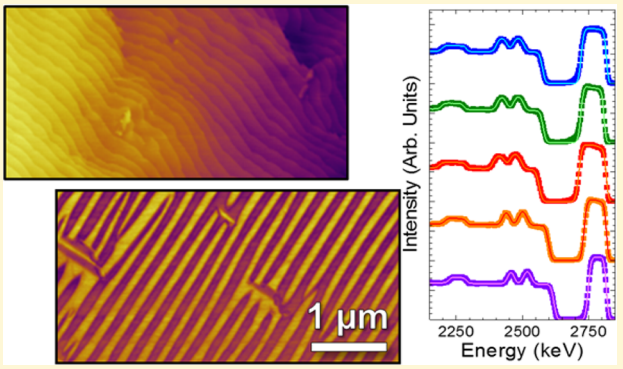

INTRODUCTION

Because of their potential for a wide range of applications, studies focused on improving synthesis of complex oxide thin films have gained momentum in recent years such that now researchers can achieve better control of film composition, strain, defect type and concentration, and ultimately material properties.[1−5] Despite these efforts, however, the ability to deterministically control the growth of these materials with the same precision applied in, for example, group IV and III−V semiconductor systems has not been achieved. This difficulty arises, in part, from the complex chemistry of these materials (i.e., the presence of multiple cation and anion species) which must be combined in the appropriate manner and maintained with exacting precision throughout the growth process. At the same time, the source materials used in the production of these complex oxides are often rather impure; achieving even 99.9% purity is expensive and difficult for many source materials. Finally, such compounds have a low energy barrier of formation for free and clustered point defects and these same point defects often form to compensate impurities or nonstoichiometry in the lattice (e.g., compensating cation vacancies with anion vacancies or vice versa). In turn, a number of recent studies have attempted to provide realistic expectations and understanding of the limits of control over the chemistry of complex oxides such as ABO_3 perovskites including $SrTiO_3$,[6−12] $LaAlO_3$,[13−17] and others.[18−21] What this work has illustrated, however, is that even as the level of control in the growth processes has improved, nonstoichiometry (both on the cation and anion sublattices) should be expected and that, in reality, a "perfect" stoichiometric film is likely the exception, not the rule.

With this said, one of the most widely studied perovskite oxides in recent history is the multiferroic $BiFeO_3$.[4,22,23] The extensive work focused on $BiFeO_3$ in the past decade has been motivated by the fact that $BiFeO_3$ simultaneously exhibits large spontaneous polarization (90−100 $\mu C/cm^2$), G-type antiferromagnetism, and the potential for strong magnetoelectric coupling. In turn, considerable effort has concentrated on the realization of a range of devices that take advantage of the multiferroic nature of this material.[22,24] Despite considerable interest and study, $BiFeO_3$ is primarily limited by one critical feature: it has poor electrical leakage performance. This leakage (arising from electronic conduction in the material under applied bias) results from the fact that $BiFeO_3$, unlike traditional ferroelectrics, has a partially populated d orbital, is rather susceptible to point defect formation (and, in turn, doping of the lattice with charge), and has a relatively small

Received: June 22, 2016
Revised: July 23, 2016
Published: July 25, 2016

DOI: 10.1021/acs.chemmater.6b02542
Chem. Mater. 2016, 28, 5952−5961

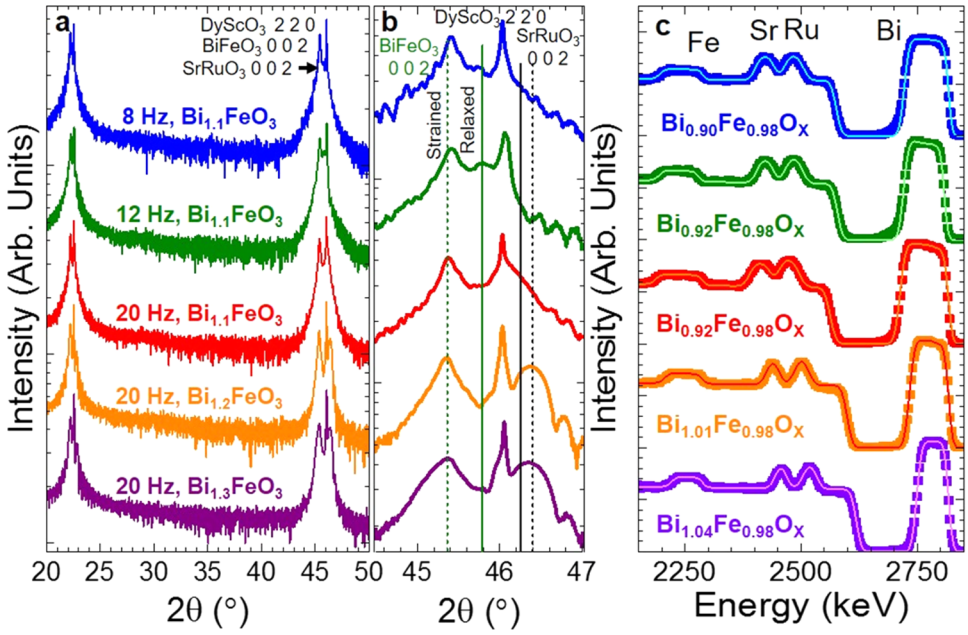

Figure 1. (a) θ–2θ X-ray diffraction patterns about the 001_{PC}- and 002_{PC}-diffraction conditions of the $BiFeO_3$ and $SrRuO_3$ films and 110- and 220-diffraction condition of the $DyScO_3$ substrate. (b) Zoom-in about the 002_{PC}- and 220-diffraction conditions showing minimal variation in the out-of-plane lattice parameter of the $BiFeO_3$ with changing growth conditions. (c) Rutherford backscattering spectroscopy (RBS) studies and the best-fit cation chemistry of the various heterostructures.

band gap compared to most ferroelectrics (band gap of 2.67 eV).[25−27] In turn, substantial efforts have explored doping/alloying of $BiFeO_3$ in an attempt to reduce the electronic leakage/conduction. For example, *A*-site doping with La and/or *B*-site doping with Ti and Cr have been shown to reduce leakage current density.[28−31] However, despite the need for deep understanding of how chemistry, defects, structure, and properties evolve in $BiFeO_3$, there has been little systematic work aimed at directly probing the role of stoichiometry in determining the crystal and domain structures and properties of $BiFeO_3$ films.[32−34]

Here, we explore how slight variations in the growth conditions of $BiFeO_3$ impact both the cation and anion chemistry, the electrical leakage, conduction mechanisms, and ferroelectric and dielectric response. Using pulsed-laser deposition, and varying laser repetition rate and target composition, films ranging in chemistry from 10% Bi-deficiency to 4% Bi-excess and Bi gradients as large a 6% across the film thickness are produced and additional variations and gradients in the O chemistry are found to follow the trends in cation chemistry. Varying film chemistry, in turn, produces marked differences in surface and domain morphology in which Bi-deficiency promotes atomically-smooth surfaces and ordered stripe domains. Large differences in leakage current density and changes in the dominant conduction mechanism including observations of heterostructures with Schottky, Poole−Frenkel, or modified Poole−Frenkel emission can be correlated to changes in both the overall cation/anion stoichiometry and gradients. Finally, Bi-excess heterostructures are found to exhibit the best low-frequency ferroelectric and dielectric response while increasing Bi-deficiency worsens the low-frequency ferroelectric performance and reduces the dielectric permittivity.

EXPERIMENTAL SECTION

$BiFeO_3$ heterostructures were grown via pulsed-laser deposition in an on-axis geometry using a KrF excimer laser (Compex, Coherent) on 30 nm $SrRuO_3$/$DyScO_3$ (110) and $LaAlO_3$ (001) or 0.5% Nb:$SrTiO_3$ (001) single-crystal substrates (CrysTec GmBH). The $SrRuO_3$ films, to be used as a bottom electrode for subsequent electrical studies, were grown at a heater temperature of 645 °C, in a dynamic oxygen pressure of 100 mTorr, with a laser energy density of 1.2 J/cm^2, and a laser repetition rate of 17 Hz from a ceramic target of composition $SrRuO_3$. The $BiFeO_3$ films were grown at a heater temperature of 700 °C, in a dynamic oxygen pressure of 100 mTorr, with a laser energy density of 1.1 J/cm^2, and as a function of laser repetition rate ranging from 8 to 20 Hz from ceramic targets of composition either $Bi_{1.1}FeO_3$, $Bi_{1.2}FeO_3$, or $Bi_{1.3}FeO_3$. To maintain consistency, even upon changing the laser repetition rate and target chemistry, 57 600 laser pulses were used to produce all $BiFeO_3$ heterostructures studied herein and resulted in films of thickness of ∼100 nm in all cases. All substrates were adhered to the heater with Ag paint (Ted Pella, Inc.), and following growth, the heterostructures were cooled to room temperature at a rate of 5 °/min in 700 Torr of oxygen.

Following growth, a variety of techniques were used to probe the structural, chemical, and electrical properties. Structural studies were performed using high-resolution X-ray diffraction and reciprocal space mapping (RSM) (Panalytical, X'pert^3 MRD). Chemical analysis was performed via Rutherford backscattering spectrometry (RBS) (incident ion energy of 3040 keV, incident angle α = 22.5°, exit angle β = 25.35°, and scattering angle θ = 168°) using the heterostructures grown on the $LaAlO_3$ (001) substrates. Fits to the experimental data were completed using the RBS analysis software SIMNRA and were evaluated using an R^2 method with $R^2 = 1 - \frac{\sum(e_i - f_i)^2}{\sum(e_i - \bar{e})^2}$, where e and f correspond to experimental and simulated data, respectively. R^2 values were calculated about the peaks of interest (i.e., for cation chemistry about the Bi and Fe peaks and for anion chemistry about the resonant O peak) to avoid artificially increasing the value of R^2 by the inclusion of substrate peaks. Film morphology and ferroelectric domain structure were imaged using atomic and piezoresponse force microscopy (PFM), respectively, with an MFP-3D microscope (Asylum Research). For electrical, dielectric,

DOI: 10.1021/acs.chemmater.6b02542
Chem. Mater. 2016, 28, 5952−5961

Table 1. Summary of Data Including Growth Conditions, Final Chemical Formula of Heterostructure, Structural (a, b, c, and β) Information, [Bi]/[Fe] Ratio, ∇[Bi], [O]/[Fe] Ratio, and ∇[O]

Growth Conditions	Chemical Formula	a	b	c	β	[Bi]:[Fe] Ratio			∇[Bi] (%)	[O]:[Fe] Ratio			∇[O] (%)
						Average	Surface	Interface		Average	Surface	Depth Limit	
8 Hz, $Bi_{1.1}FeO_3$ Target	$Bi_{0.90}Fe_{0.98}O_{2.49}$	3.950	3.941	4.019	89.62	0.90 : 0.98	0.90 : 0.98	0.91 : 0.98	1	2.49 : 0.98	2.49 : 0.98	2.49 : 0.98	0
12 Hz, $Bi_{1.1}FeO_3$ Target	$Bi_{0.92}Fe_{0.98}O_{2.67}$	3.948	3.933	4.020	89.61	0.92 : 0.98	0.91 : 0.98	0.94 : 0.98	3	2.67 : 0.98	2.64 : 0.98	2.70 : 0.88	2
20 Hz, $Bi_{1.1}FeO_3$ Target	$Bi_{0.92}Fe_{0.98}O_{2.70}$	3.947	3.938	4.016	89.60	0.92 : 0.98	0.89 : 0.98	0.95 : 0.98	6	2.70 : 0.98	2.67 : 0.98	2.73 : 0.98	4
20 Hz, $Bi_{1.2}FeO_3$ Target	$Bi_{1.01}Fe_{0.98}O_{2.97}$	3.955	3.932	4.013	89.63	1.01 : 0.98	1.01 : 0.98	1.01 : 0.98	0	2.97 : 0.98	2.97 : 0.98	3.00 : 0.98	1
20 Hz, $Bi_{1.3}FeO_3$ Target	$Bi_{1.04}Fe_{0.98}O_{3.00}$	3.951	3.947	4.021	89.63	1.04 : 0.98	1.04 : 0.98	1.04 : 0.98	0	3.00 : 0.98	2.97 : 0.98	3.00 : 0.98	1

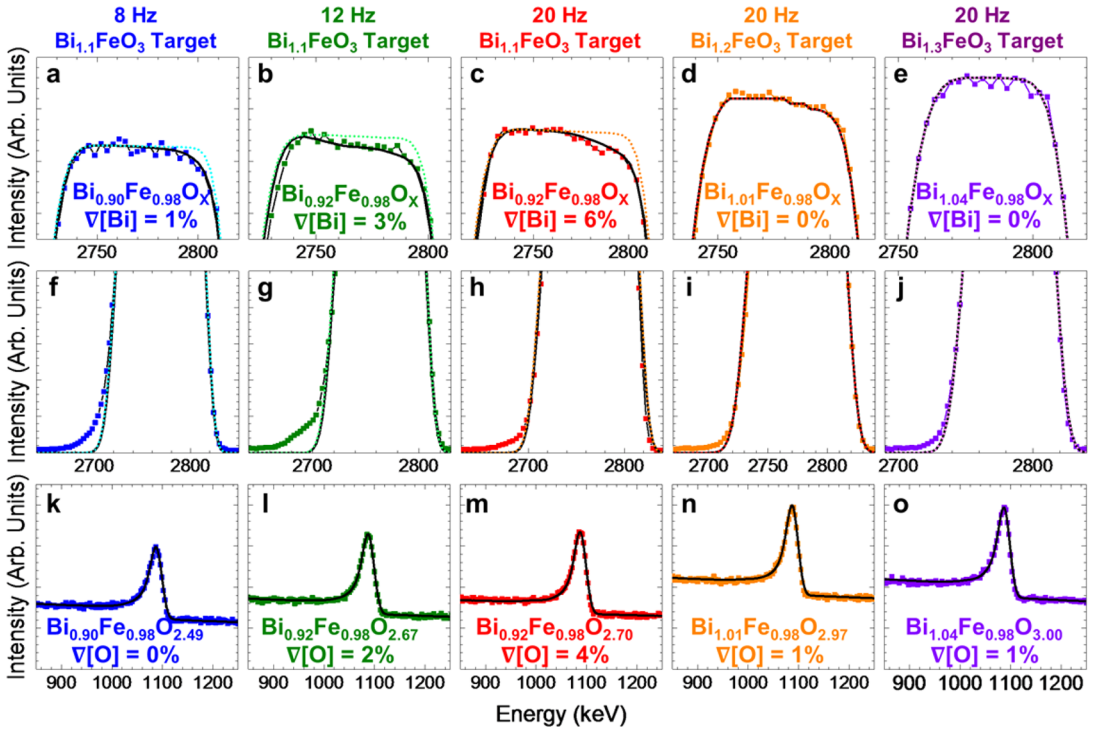

Figure 2. Enlarged view of the (a–e) top of the Bi RBS peak, (f–j) the low-energy, leading edge of the Bi RBS peak, and (k–o) the O resonance RBS peak for the (a, f, and k) $Bi_{0.90}Fe_{0.98}O_{2.49}$, (b, g, and l) $Bi_{0.92}Fe_{0.98}O_{2.67}$, (c, h, and m) $Bi_{0.92}Fe_{0.98}O_{2.70}$, (d, i, and n) $Bi_{1.01}Fe_{0.98}O_{2.97}$, and (e, j, and o) $Bi_{1.04}Fe_{0.98}O_{3.00}$ heterostructures, respectively.

and ferroelectric studies, symmetric capacitor structures were fabricated by *ex situ* deposition of 80 nm thick $SrRuO_3$ top electrodes defined using a MgO hard-mask process.[35] Current–voltage (leakage) measurements were performed using a 6517B electrometer (Keithley/Tektronix), ferroelectric polarization hysteresis loops were measured using a Precision Multiferroic Tester (Radiant Technologies), and dielectric and loss tangent measurements were performed using an E4890 LCR meter (Agilent/Keysight) for frequencies up to 1 MHz.

RESULTS AND DISCUSSION

We begin by discussing the X-ray diffraction results. Wide angle θ–2θ scans reveal that all $BiFeO_3$ heterostructures are fully epitaxial, 00*l*-oriented, and single-phase (Figure 1a). Closer examination of the 002_{PC}-diffraction condition of $BiFeO_3$ (where PC refers to pseudocubic notation) reveals essentially no change in the peak position or shape of the diffraction peak despite changing growth conditions (Figure 1b). Rocking curves about the 002_{PC}- and 220-diffraction conditions of the film and substrate, respectively, were used to examine the crystal quality of the heterostrctures (Supporting Information, Figure S1). In all cases, the full width at half-maximum (fwhm) of the films is between ∼2–5 times that of the substrate indicating comparable crystal quality. Asymmetric RSMs about the 103_{PC}- (Supporting Information, Figure S2), 203_{PC}-, and $0\bar{2}3_{PC}$- (Supporting Information, Figure S3) diffraction conditions of the film and substrate were used to examine the strain state of the heterostructures and to obtain the lattice parameters of the films (a, b, c, and β; Table 1); in all cases the films are essentially coherently strained to the substrate. Subsequent studies of heterostructure stoichiometry via RBS (Figure 1c) reveal, unsurprisingly, that both changing the laser repetition rate, while maintaining a constant target composition, and changing the target composition, while maintaining a constant laser repetition rate, results in changes in the average film chemistry. In general, upon increasing the laser repetition rate (and using, for example, the $Bi_{1.1}FeO_3$ target), the average chemistry is Bi-deficient and changes only slightly but becomes richer in Bi. On the other hand, upon increasing the Bi content in the target (and maintaining a laser repetition rate of 20 Hz), the average chemistry goes from Bi-deficient ($Bi_{0.92}Fe_{0.98}O_x$, for growth from a $Bi_{1.1}FeO_3$ target) to nearly stoichiometric ($Bi_{1.01}Fe_{0.98}O_x$, for growth from a $Bi_{1.2}FeO_3$ target) to Bi-excess ($Bi_{1.04}Fe_{0.98}O_x$, for growth from a $Bi_{1.3}FeO_3$ target). A complete summary of the average heterostructure cation stoichiometry for all variants is provided (wherein the Bi and Fe concentrations are noted as [Bi] and [Fe] and the values

DOI: 10.1021/acs.chemmater.6b02542
Chem. Mater. 2016, 28, 5952–5961

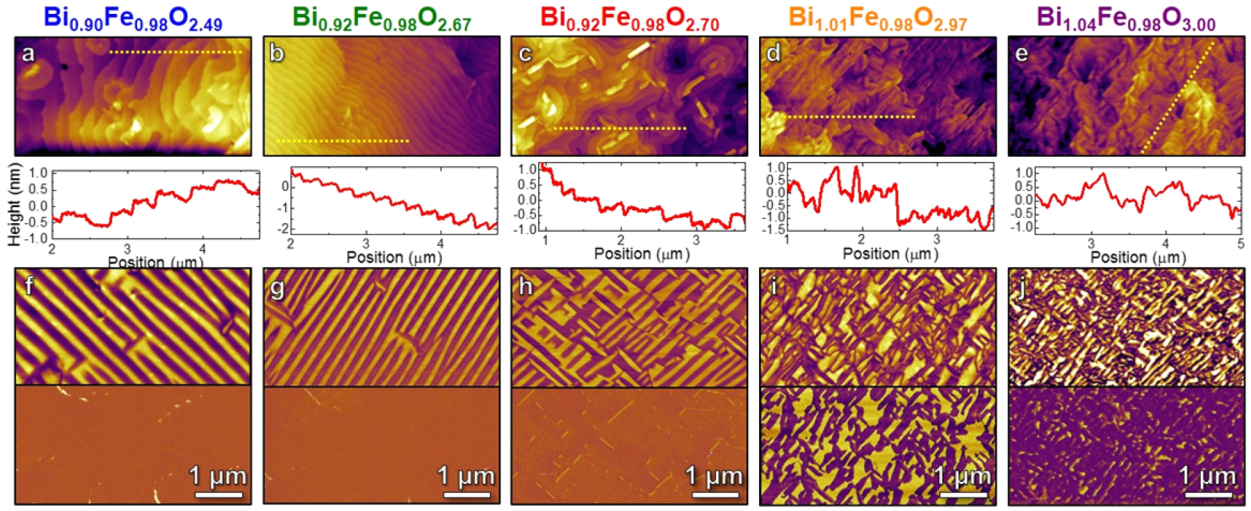

Figure 3. Atomic force microscopy images (top) and line traces (done at the yellow dashed line, bottom) for the (a) $Bi_{0.90}Fe_{0.98}O_{2.49}$, (b) $Bi_{0.92}Fe_{0.98}O_{2.67}$, (c) $Bi_{0.92}Fe_{0.98}O_{2.70}$, (d) $Bi_{1.01}Fe_{0.98}O_{2.97}$, and (e) $Bi_{1.04}Fe_{0.98}O_{3.00}$ heterostructures. Lateral (top) and vertical (bottom) piezoresponse force microscopy amplitude for the (f) $Bi_{0.90}Fe_{0.98}O_{2.49}$, (g) $Bi_{0.92}Fe_{0.98}O_{2.67}$, (h) $Bi_{0.95}Fe_{0.98}O_{2.70}$, (i) $Bi_{1.01}Fe_{0.98}O_{2.97}$, and (j) $Bi_{1.04}Fe_{0.98}O_{3.00}$ heterostructures.

reported represent the fraction of occupation of the ideal chemistry; [Bi]:[Fe] ratio, Table 1).

Closer examination of the RBS data reveals that, in addition to variations in the average cation chemistry of the heterostructures, the different structures also exhibit inhomogeneous cation stoichiometry throughout the thickness of the film (Figure 2a–e). In general, the lower the laser repetition rate and/or the higher the Bi content of the target, the smaller the gradient in the cation chemistry in the heterostructure. Additionally, heterostructures with a gradient in [Bi] (noted as ∇[Bi]) across the film thickness (Figure 2a–c) show a smeared low-energy edge of the Bi peak in the RBS spectra (Figure 2f–h) that indicates a diffuse $BiFeO_3/SrRuO_3$ interface. We hypothesize that the initial material incident on the substrate matches (within reason) the starting target stoichiometry (in all cases, $Bi_{1.1}FeO_3$) but that, due to the relatively high vapor pressure of the Bi, Bi adatoms begin to volatilize from the surface of the growing film at a nontrivial rate. In turn, the nature of the [Bi] in the film depends on this adatom attachment/detachment rate which is also dependent on the rate of growth. In other words, the slower the growth (i.e., the lower the laser repetition rate), the more Bi can desorb from the surface during the growth simply because it is exposed to high temperatures for longer time periods. In turn, the surface becomes Bi-deficient, and there is now a driving force for diffusion of the Bi from deeper in the film toward the surface. As a result, the heterostructures grown at low laser repetition rates exhibit the most Bi-deficiency, but this also drives a reduction in the ∇[Bi] since there is more time for the system to reach equilibrium by diffusing Bi from deeper in the film (Figure 2a–e). Furthermore, it appears that not only does the gradient in [Bi] drive diffusion of Bi from deeper in the film to the surface, but it can also drive Bi diffusion into the underlying $SrRuO_3$ as it attempts to normalize/homogenize the [Bi] in the film. This, in turn, helps explain both the pronounced interfacial diffusivity at the $BiFeO_3/SrRuO_3$ interface (Figure 2f–h) and is consistent with the θ–2θ scans (Figure 1b) and RSMs (Supporting Information, Figures S2 and S3) which show expansion of the $SrRuO_3$ out-of-plane lattice parameter as would occur with Bi incorporation. Thus, increasing the laser repetition rate (or shortening the deposition time) can drive the average [Bi] up, but at the expense of creating larger ∇[Bi] for a given target composition. This trend can be reduced, however, by growing at high laser repetition rates from highly-Bi-excess targets (Figure 2d,e and i,j) where the adatom attachment/detachment rate is such that the [Bi] can be maintained close to stoichiometry without formation of any measurable ∇[Bi]; akin to what is achieved in adsorption-controlled growth of $BiFeO_3$ via molecular beam epitaxy.[36]

Beyond just probing the cation chemistry, RBS can also be used to investigate the anion chemistry. In particular, we completed studies at the O resonance energy (3.04 MeV) wherein the O has an increased scattering cross-section which results in high intensities and surface-sensitive information (Figure 2k–o). Subsequent fitting of the O resonance peaks, in turn, provides information about the nature of O stoichiometry in the heterostructures. We note, however, that for studies of the resonance peaks that the fits are relatively sensitive to a number of input parameters and that utilization of a scattering cross-section[37] for the exact geometry of the instrument is key in obtaining reliable information. Furthermore, to limit the influence of nonresonant scattering from oxygen in the substrate, the energy loss of the incident He^{2+} ions as they transit through the heterostructure thickness was calculated using SRIM[38] and compared to the 0.01 MeV full-width at half-maximum of the O scattering cross-section. The He^{2+} ions were found to lose 0.01 MeV upon transiting through the first 45 nm of the heterostructure from the surface. Thus, 45 nm was considered to be the depth limit for resonant peak fitting and only information pertaining to the top 45 nm of all heterostructures was used to quantify the O stoichiometry. Finally, although we are confident with cation chemistries to ~1–2% accuracy (that is a change of $A_1B_1O_3$ cation chemistry by 0.01 out of 1), difficulty in fitting the low-energy tail of the resonant peaks renders accurate reporting to better than ~3% (that is a change of $A_1B_1O_3$ anion chemistry of 0.1 out of 3) difficult. From these studies, we observe that both the average ([O]) and gradient (∇[O]) in anion stoichiometry are seemingly coupled to the corresponding [Bi] and ∇[Bi]

DOI: 10.1021/acs.chemmater.6b02542
Chem. Mater. 2016, 28, 5952–5961

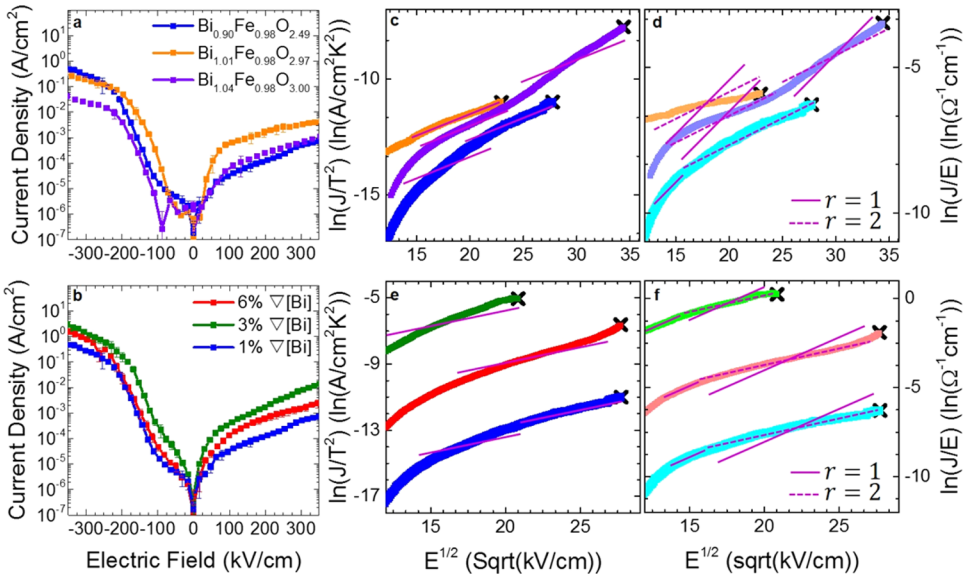

Figure 4. Current−voltage (I−V) characteristics for heterostructures of (a) varying average [Bi] but little to no ∇[Bi] and (b) little to no change in average [Bi] but varying ∇[Bi]. (c) Schottky emission and (d) Poole−Frenkel (r = 1, solid lines) and modified Poole−Frenkel (r = 2, dashed lines) emission fits for heterostructures with varying average [Bi] but little to no ∇[Bi] as shown in part (a). (e) Schottky emission and (f) Poole−Frenkel (r = 1, solid lines) and modified Poole−Frenkel (r = 2, dashed lines) emission fits for heterostructures with little to no change in average [Bi] but varying ∇[Bi] as shown in part (b). In all cases, the lines show the slope required to produce a $K = n^2 = 6.25$.

wherein Bi-deficiency results in corresponding O-deficiency (Table 1). Such coupled behavior is expected since the O chemistry can be used to compensate for cation non-stoichiometry to maintain charge neutrality in the system. In general, we find that in most heterostructure variants there is an average O-deficiency and that there is also a ∇[O] that is similar in magnitude to the ∇[Bi]. In the most Bi-deficient heterostructures, the measured [O] suggests that the concentration of O-vacancies closely meets the requisite amount required for achieving charge neutrality in relation to the concentration of Bi-vacancies.

Thus, we have seen that even though the structural studies show little variation in the crystallinity or lattice parameter of the $BiFeO_3$ heterostructures, large changes in stoichiometry may be occurring. Subsequent studies of the film morphology and domain structure evolution also reveal marked differences with [Bi] and ∇[Bi] (Figure 3). The morphology of the most Bi-deficient heterostructure ($Bi_{0.90}Fe_{0.98}O_{2.49}$; Figure 3a) is the most pristine (i.e., exhibiting atomic-level terraces and a root-mean-squared (RMS) roughness of only 300 pm), but upon increasing the average [Bi] the RMS roughness is found to increase systematically (from 354 to 525 pm to 584 pm for heterostructures with average stoichiometry $Bi_{0.92}Fe_{0.98}O_{2.67}$ (Figure 3b), $Bi_{0.92}Fe_{0.98}O_{2.70}$ (Figure 3c), and $Bi_{1.01}Fe_{0.98}O_{2.97}$ (Figure 3d), respectively), before reducing again to 407 pm as the stoichiometry trends toward Bi-excess in the $Bi_{1.04}Fe_{0.98}O_{3.00}$ heterostructure (Figure 3e). Another difference is highlighted by line traces across the different surfaces (yellow dashed line and bottom, Figure 3a−e). The $Bi_{0.90}Fe_{0.98}O_{2.49}$ (Figure 3a), $Bi_{0.92}Fe_{0.98}O_{2.67}$ (Figure 3b), and $Bi_{0.92}Fe_{0.98}O_{2.70}$ (Figure 3c) heterostructures exhibit step heights consistent with a full unit cell (3.9−4.1 Å), while the $Bi_{1.01}Fe_{0.98}O_{2.97}$ (Figure 3d) and $Bi_{1.04}Fe_{0.98}O_{3.00}$ (Figure 3e) heterostructures exhibit step heights indicative of half unit-cell steps (1.8−2.1 Å). The implications of this change in the surface morphology will be discussed more later.

At the same time, the domain structure of the heterostructures is also seen to evolve with film chemistry wherein three distinct domain structures are observed using PFM. First, primarily two-variant, stripe-domain structures with 71° domain walls are observed wherein lateral (top) and vertical (bottom) signals reveal stripe-like and uniform contrast, respectively, for the $Bi_{0.90}Fe_{0.98}O_{2.49}$ (Figure 3f) and $Bi_{0.92}Fe_{0.98}O_{2.67}$ (Figure 3g) heterostructures. The second type of domain structure corresponds to a degradation of the two-variant, stripe-domain structure into a four-variant, stripe-domain structure, again with 71° domain walls as indicated by a more complex lateral (top, Figure 3h) but still uniform vertical signal (bottom, Figure 3h) as in the $Bi_{0.92}Fe_{0.98}O_{2.70}$ heterostructure. Finally, the third type of domain structure is an evolution into a much more complex, mosaic-like domain structure with a mixture of both 71° and 109° (and potentially 180°) domain walls as indicated by a complex, mixed contrast in both the lateral (top) and vertical (bottom) signals for the $Bi_{1.01}Fe_{0.98}O_{2.97}$ (Figure 3i) and $Bi_{1.04}Fe_{0.98}O_{3.00}$ (Figure 3j) heterostructures.

This domain evolution is, at first glance, somewhat unexpected since all heterostructures are grown on similar $DyScO_3$ substrates with the same starting $SrRuO_3$ bottom electrode. Deeper inspection, however, reveals some potential explanations. First, recall from the RBS spectra (Figure 2) that the $Bi_{0.90}Fe_{0.98}O_{2.49}$, $Bi_{0.92}Fe_{0.98}O_{2.67}$, and $Bi_{0.92}Fe_{0.98}O_{2.70}$ heterostructures all show both the lowest [Bi] and the highest Bi-diffusion into the $SrRuO_3$ bottom electrode. We hypothesize that this alloying/mixing during growth creates a diffuse interfacial "virtual substrate" for the subsequent growth of the $BiFeO_3$. This buffer layer accomplishes a number of important tasks including smearing out the interface and thus the effects of varying interfacial termination, creates a homogeneous electronic structure at the interface, and finally structurally adjusts to provide for the down-selection to a single structural variant in the $BiFeO_3$. At the same time, these heterostructures are also the most nonstoichiometric and thus have the highest concentration of potential screening charges. These two

DOI: 10.1021/acs.chemmater.6b02542
Chem. Mater. 2016, 28, 5952−5961

features together, in turn, promote the formation of two-variant domain structures and uniform out-of-plane polarization.[39,40] As the heterostructures tend toward stoichiometry and both the concentration of screening charges and the interfacial interdiffusion is reduced, we would expect both a more abrupt $BiFeO_3/SrRuO_3$ interface and a stronger dependence of the polarization on the screening potential of the bottom electrode (as opposed to self-screening via carriers in the ferroelectric). In this work, we have not treated the $DyScO_3$ substrates prior to growth and thus they are expected to exhibit mixed-termination and, thus, favor mixed-termination $SrRuO_3$.[41] Mixed-termination in $SrRuO_3$ is important as prior work has demonstrated that variations in the termination of the bottom electrode can drive $BiFeO_3$ to form either up- or down-polarized domains depending on the interfacial structure.[42] This could be responsible for the observation of mixed contrast in the vertical PFM signal (bottom, Figure 3i,j). This hypothesis is further supported by the presence of the half unit-cell steps on the surfaces of the $Bi_{1.01}Fe_{0.98}O_{2.97}$ and $Bi_{1.04}Fe_{0.98}O_{3.00}$ heterostructures (Figure 3d,e). This is, in turn, exacerbated by the fact that these films are closer to ideal stoichiometry and thus the concentration of charged defects capable of self-screening the polarization is reduced meaning the direction of polarization is more sensitive to the underlying bottom electrode.

From here, we proceed to explore how the variations in chemistry impact the evolution of electronic, dielectric, and ferroelectric properties. Because of the wide range of [Bi] in the heterostructures, test devices were grown on 0.5% Nb:$SrTiO_3$ to confirm the nature of the majority carrier type in each heterostructure. In all cases, the $BiFeO_3$/Nb:$SrTiO_3$ interface is Ohmic in nature, while the $BiFeO_3/SrRuO_3$ interface is a Schottky junction. A schematic band diagram and current−voltage data are provided (Supporting Information, Figure S4) which enable us to state that, in all cases, the conduction in the $BiFeO_3$ is *n*-type in nature. Focusing now on the current−voltage (leakage) studies on the various $BiFeO_3/SrRuO_3$ heterostructures (Figure 4a,b), in all cases, similar leakage behavior is observed from the standpoint of both form and magnitude. Looking at those heterostructures found to possess little or no ∇[Bi] but systematic changes in the average [Bi] we find that under both positive and negative bias, the stoichiometric $Bi_{1.01}Fe_{0.98}O_{2.97}$ heterostructures exhibit the highest leakage (Figure 4a). Although this is perhaps counter to what would be desired from the most "ideal" film, it is actually expected due to the low concentration of compensating acceptor states relative to the intrinsic O-vacancy concentration. In turn, as one transitions to either Bi-excess or Bi-deficiency, the leakage is reduced. We find that the leakage behavior is nearly identical in both the Bi-deficient ($Bi_{0.90}Fe_{0.98}O_{2.49}$) and Bi-excess ($Bi_{1.04}Fe_{0.98}O_{3.00}$) heterostructures due to the relatively high cation vacancy concentrations in both heterostructures which act to compensate the oxygen vacancies and thus reduce free charge carrier densities. Similar studies for heterostructures exhibiting both overall average Bi-deficiency and varying ∇[Bi] (Figure 4b) reveal similar leakage behavior (albeit with slightly different leakage current densities). Under negative bias, the heterostructures with ∇[Bi] show similar leakage current densities which is consistent with the uniformity in surface chemistry of all three films (Table 1). Under positive bias, the leakage response is similar in shape and the magnitude seems to increase with increasing ∇[Bi].

Further analysis of the current−voltage data was undertaken to understand the nature of electronic transport in the heterostructures (Figure 4c−f). As part of this analysis we have considered a number of potential transport mechanisms including Schottky emission, classic Poole−Frenkel emission, modified Poole−Frenkel emission, and space charge limited conduction. To briefly summarize, Schottky emission describes a transport process dictated by interfacial electronic structure in the form of a Schottky barrier that must be overcome to enable charge transport.[43] Poole−Frenkel emission, on the other hand, describes transport dictated by field-assisted emission from internal trap states in a material.[44] Poole−Frenkel emission can, however, be more complex in the presence of multiple trap states and thus a so-called modified Poole−Frenkel emission model was developed wherein an exponential scaling term is added to account for a situation in which there are large concentrations of both donor and/or acceptor states in a material.[45,46] In such cases, the classic Poole−Frenkel equation is modified by a constant r ($1 \leq r \leq 2$) which modifies the slope obtained from the log (J/E) vs $E^{1/2}$ plots. The dielectric constant obtained from the slope can range from that of the traditional Poole−Frenkel model ($r = 1$) to values one-fourth as large ($r = 2$), depending on the relative concentration of donor and acceptor states. Finally, space charge limited conduction describes a transport mechanism in which the rate of charge injection into the film outpaces the bulk charge transport such that a limiting space charge is formed which governs overall behavior.[47,48] Details of the fitting procedures for each of these mechanisms are provided (Supporting Information). To aid in understanding the relative merits of each fitting procedure, the experimental data have been overlaid with lines of slope corresponding to a dielectric constant $K = n^2 = 6.25$ as reported previously in the literature for $BiFeO_3$.[49,50]

This analysis, in turn, provides a number of important observations. First, all heterostructure variants are clearly not governed by space charge limited conduction (Supporting Information, Figure S5). Second, despite overall similar leakage current shape and magnitude, the results fall into one of three different classes of behavior. For stoichiometric heterostructures ($Bi_{1.01}Fe_{0.98}O_{2.97}$), the best fit is for Schottky emission (orange data, Figure 4c). Comparison with a Poole−Frenkel or modified Poole−Frenkel emission fit (orange data, Figure 4d) shows a poor agreement with the experimental data. For the low ∇[Bi], Bi-deficient ($Bi_{0.90}Fe_{0.98}O_{2.49}$) and Bi-excess ($Bi_{1.04}Fe_{0.98}O_{3.00}$) heterostructures, fits to the Schottky emission model (blue and purple data, Figure 4c) are in poor agreement with the experimental data and, instead, these heterostructures are best fit with something between a classic Poole−Frenkel and modified Poole−Frenkel behavior (blue and purple data, Figure 4d). This trend toward the modified Poole−Frenkel behavior is consistent with the fact that these heterostructures have large concentrations of defects from nonstoichiometry and, in turn, should exhibit large concentrations of both acceptor and/or donor states. For the heterostructures exhibiting both overall average Bi-deficiency and varying ∇[Bi], a more complex evolution is observed (Figure 4e,f). To begin, these heterostructures are clearly not well fit to Schottky emission in any field regime. Investigation of fits to Poole−Frenkel and modified Poole−Frenkel emission reveals that the heterostructures are generally better fit to classical Poole−Frenkel behavior at low fields and that the transport evolves to be better fit by the modified Poole−Frenkel behavior at high field regimes (Figure 4f). Such behavior is likely

DOI: 10.1021/acs.chemmater.6b02542
Chem. Mater. 2016, 28, 5952−5961

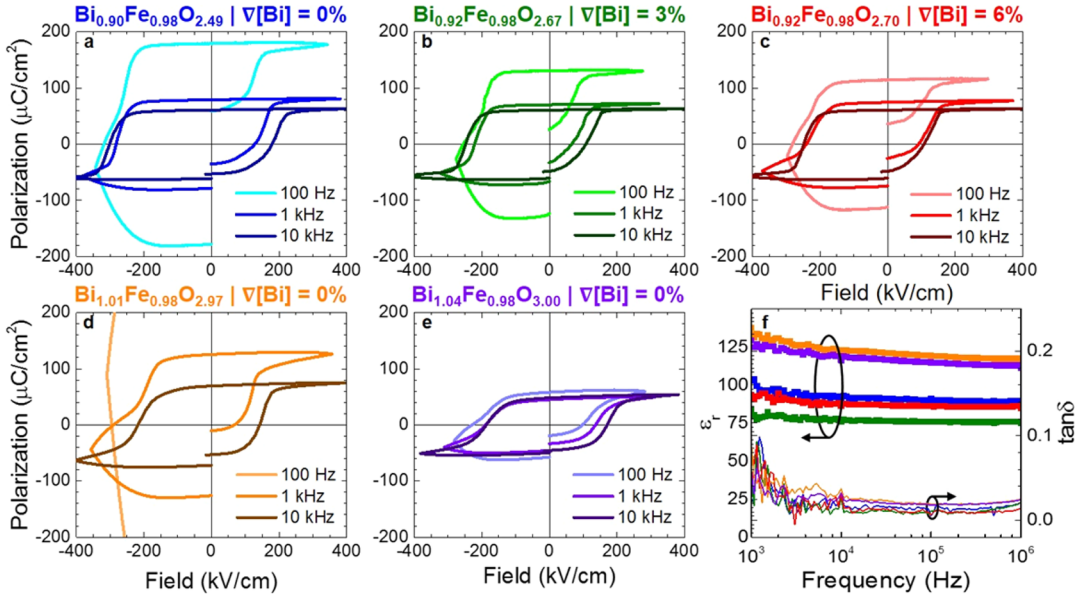

Figure 5. Ferroelectric hysteresis loops measured at 0.1, 1, and 10 kHz for (a) $Bi_{0.90}Fe_{0.98}O_{2.49}$, (b) $Bi_{0.92}Fe_{0.98}O_{2.67}$, (c) $Bi_{0.92}Fe_{0.98}O_{2.70}$, (d) $Bi_{1.01}Fe_{0.98}O_{2.97}$, and (e) $Bi_{1.04}Fe_{0.98}O_{3.00}$ heterostructures. (f) Frequency-dependence of dielectric permittivity (left axis) and loss tangent (right axis) for all heterostructures (colors match other data).

explained by the presence of a gradient in both the cation and anion defect concentration and thus transport through the two interfaces and/or various portions of the film are different as the defect type and concentration changes. Again, the transition from classic Poole−Frenkel to modified Poole−Frenkel behavior is likely when the concentration of compensating donor states is nontrivial.[45,46]

Clearly the change in stoichiometry has a large role to play in the evolution of electronic conduction mechanism and magnitude. It is, in turn, expected that this will have important implications for the evolution of ferroelectric response. Using the same symmetric capacitor structures used for the current−voltage studies, ferroelectric hysteresis loops were measured at a range of frequencies (for brevity data at 0.1, 1, and 10 kHz are provided; Figure 5a−e). Much like the current−voltage response, the data can be grouped into three major categories. First, the stoichiometric heterostructures show the "worst" ferroelectric hysteresis loops (i.e., largest leakage current contribution to polarization, unclosed loops, etc.) (Figure 5d). This is, in the context of the leakage current data, unsurprising since these heterostructures exhibit the largest leakage response. Again, the low cation vacancy concentration in the stoichiometric heterostructures seems to allow for uncompensated *n*-type carriers (arising from compensation of the oxygen vacancies) to dominate the overall leakage behavior thus rendering loops measured below ∼1 kHz unmeasurable. Second, upon transitioning to slightly Bi-deficient ($Bi_{0.92}Fe_{0.98}O_{2.70}$) and Bi-excess ($Bi_{1.04}Fe_{0.98}O_{3.00}$) heterostructures, there is marked improvement in the nature of the ferroelectric hysteresis loops wherein in most cases and frequencies it is possible to obtain saturated loops in both directions (Figure 5c,e). Compared to the stoichiometric heterostructures, both the Bi-deficient and Bi-excess heterostructures exhibit lower overall leakage currents (Figure 4a,b) and thus this improvement in leakage current manifests as better overall ferroelectric response. The third observation, however, is that low leakage current alone is not enough to maintain robust ferroelectric response. Upon transitioning to highly Bi-deficient heterostructures ($Bi_{0.90}Fe_{0.98}O_{2.49}$ and $Bi_{0.92}Fe_{0.98}O_{2.67}$) the loops again begin to show more signatures of strong leakage components and more difficulty in achieving saturation in both applied field directions (Figure 5a,b). Unlike the current−voltage data, however, things are slightly more complex. In this case the role of the ∇[Bi] seems to be important in that those heterostructures with lower ∇[Bi] exhibit worse ferroelectric response. For example, comparison of the $Bi_{0.92}Fe_{0.98}O_{2.67}$, ∇[Bi] = 3% (Figure 5b) and $Bi_{0.92}Fe_{0.98}O_{2.70}$, ∇[Bi] = 6% (Figure 5c) heterostructures reveals that the heterostructure with lower ∇[Bi] has a tendency to show higher leakage. This likely suggests an important role of the chemical gradients in reducing conduction in the films.

Furthermore, there is a trend in the coercive field with stoichiometry in the $BiFeO_3$ heterostructures. The most Bi-deficient ($Bi_{0.90}Fe_{0.98}O_{2.49}$, ∇[Bi] = 0%) heterostructures exhibit the largest average coercive field (∼235 kV/cm, Figure 5a), which is consistent with domain pinning due to the high concentration of both point defects. All other heterostructure variants have comparable average coercive fields (∼170 kV/cm, Figure 5b−e). The difference, instead, comes in the horizontal shift of the hysteresis loops. A noticeable horizontal shift of ∼140 kV/cm is observed in both heterostructures exhibiting the largest ∇[Bi] [namely, $Bi_{0.92}Fe_{0.98}O_{2.67}$, ∇[Bi] = 3% (Figure 5b) and $Bi_{0.92}Fe_{0.98}O_{2.70}$, ∇[Bi] = 6% (Figure 5c)], but horizontal shifts are not observed in the heterostructures with more ideal stoichiometry and minimal ∇[Bi] [namely, $Bi_{1.01}Fe_{0.98}O_{2.97}$, ∇[Bi] = 0% (Figure 5d) and $Bi_{1.04}Fe_{0.98}O_{3.00}$, ∇[Bi] = 0% (Figure 5e)]. There are two possible explanations for these horizontal shifts (or built-in potentials) in the nonhomogeneous heterostructures. First, the Schottky barrier heights at the top and bottom interfaces could be different due to changes in the chemistry at the top and bottom interfaces, thus, producing an asymmetric electrode structure which can induce voltage shifts in ferroelectric hysteresis loops.[51,52] Second, the presence of chemical gradients in the film could results in innate symmetry breaking and the formation of

DOI: 10.1021/acs.chemmater.6b02542
Chem. Mater. 2016, 28, 5952−5961

higher-order phenomena which can break even-order symmetry in ferroelectrics which manifests as built-in potentials (e.g., flexo-chemo-electric effects in compositionally graded ferroelectrics).[53]

Finally, we have also examined the impact of stoichiometry on the evolution of dielectric permittivity and loss (Figure 5f). Bulk $BiFeO_3$ is expected to exhibit a dielectric permittivity of ~110 (at low frequencies).[54] Despite showing among the highest leakage currents and the worst ferroelectric response, the stoichiometric ($Bi_{1.01}Fe_{0.98}O_{2.97}$, $\nabla[Bi]$ = 0%) heterostructures (orange data, Figure 5f) show essentially bulk-like dielectric behavior and low tan δ. This is consistent with observations for a number of other perovskite phases in recent work wherein only nearly stoichiometric versions of materials show the expected dielectric permittivity.[10,16] The Bi-excess ($Bi_{1.04}Fe_{0.98}O_{3.00}$, $\nabla[Bi]$ = 0%) heterostructures (purple data, Figure 5f) also show nearly ideal dielectric permittivity, consistent with prior work on Bi-excess (up to 10% excess) ceramics wherein bulk-like dielectric permittivity was observed.[34] Upon moving to Bi-deficiency and/or in the presence of $\nabla[Bi]$, however, the dielectric permittivity falls dramatically and the variants show a trend inverse to that from the leakage response (Figure 4d). The reduced dielectric permittivity may be explained by the fact that these heterostructures exhibit the most extensive interfacial interdiffusion and we propose that this interdiffusion creates a region of lower capacitance which dominates the dielectric response of the films.

CONCLUSIONS

We have demonstrated that laser repetition rate and target composition have a significant effect on the average [Bi] and $\nabla[Bi]$ in thin films and that this variation has important implications for the evolution of material properties. In particular, we observe the ability to produce single-phase, coherently strained films despite having film chemistries that range from 10% Bi-deficiency to 4% Bi-excess and possessing $\nabla[Bi]$ as large a 6% across the film thickness. In-depth RBS studies reveal corresponding variations and gradients in the O chemistry. As a result of the varying film chemistry, marked differences in surface and domain morphology are observed wherein Bi-deficiency stabilizes atomically smooth surfaces and ordered stripe domains. The formation of complex, mosaic-like domains is attributed to films that are more sensitive to the interfacial crystal and electronic structure. Subsequent investigation of current−voltage response reveals large differences in leakage current density arising from changes in both the overall stoichiometry and gradients and the manifestation of three different transport mechanisms including Schottky, Poole−Frenkel, and modified Poole−Frenkel emission responses. This, in turn, results in variations in the quality of ferroelectric hysteresis loops wherein slightly Bi-deficient and Bi-excess heterostructures are found to exhibit the best low-frequency ferroelectric response. Study of the dielectric permittivity finds nearly bulk-like response in stoichiometric and Bi-excess films and permittivity that reduces with Bi-deficiency. All told, the current work provides one of the most detailed and systematic studies of chemistry and property evolution in thin films of the important multiferroic $BiFeO_3$. With the trends and insights gleaned from this work, it should be possible to prescribe routes to garner better control of $BiFeO_3$ films in device structures which could, in turn, open the door to utilize this complex but multifaceted material in next-generation applications.

ASSOCIATED CONTENT

Supporting Information

The Supporting Information is available free of charge on the ACS Publications website at DOI: 10.1021/acs.chemmater.6b02542.

Full information about rocking curves, reciprocal space maps, n-type conduction, and conduction mechanism fitting for relevant heterostructures (PDF)

AUTHOR INFORMATION

Corresponding Author

*E-mail: lwmartin@berkeley.edu.

Notes

The authors declare no competing financial interest.

ACKNOWLEDGMENTS

L.R.D. acknowledges support from the U.S. Department of Energy under Grant No. DE-SC0012375. S.S. acknowledges support from the National Science Foundation under Grant CMMI-1434147. Z.C. acknowledges partial support from the Air Force Office of Scientific Research under Grant FA9550-12-1-0471 and the Laboratory Directed Research and Development Program of Lawrence Berkeley National Laboratory under U.S. Department of Energy Contract No. DE-AC02-05CH11231. A.R.D. acknowledges support from the Army Research Office under Grant W911NF-14-1-0104. R.G. acknowledges support from the National Science Foundation under Grant OISE-1545907. L.W.M. acknowledges support from the National Science Foundation under Grant DMR-1451219.

REFERENCES

(1) Chambers, S. A. Epitaxial Growth and Properties of Thin Film Oxides. *Surf. Sci. Rep.* **2000**, *39*, 105−180.
(2) Schlom, D. G.; Chen, L.-Q.; Eom, C.-B.; Rabe, K. M.; Streiffer, S. K.; Triscone, J.-M. Strain Tuning of Ferroelectric Thin Films. *Annu. Rev. Mater. Res.* **2007**, *37*, 589−626.
(3) Martin, L. W.; Ramesh, R. Multiferroic and Magnetoelectric Heterostructures. *Acta Mater.* **2012**, *60*, 2449−2470.
(4) Martin, L. W.; Schlom, D. G. Advanced Synthesis Techniques and Routes to New Single-Phase Multiferroics. *Curr. Opin. Solid State Mater. Sci.* **2012**, *16*, 199−215.
(5) Schlom, D. G. Perspective: Oxide Molecular-Beam Epitaxy Rocks! *APL Mater.* **2015**, *3*, 062403.
(6) Ohnishi, T.; Lippmaa, M.; Yamamoto, T.; Meguro, S.; Koinuma, H. Improved Stoichiometry and Misfit Control in Perovskite Thin Film Formation at a Critical Fluence by Pulsed Laser Deposition. *Appl. Phys. Lett.* **2005**, *87*, 241919.
(7) Ohnishi, T.; Shibuya, K.; Yamamoto, T.; Lippmaa, M. Defects and Transport in Complex Oxide Thin Films. *J. Appl. Phys.* **2008**, *103*, 103703.
(8) Keeble, D. J.; Wicklein, S.; Dittmann, R.; Ravelli, L.; Mackie, R. A.; Egger, W. Identification of a- and B-Site Cation Vacancy Defects in Perovskite Oxide Thin Films. *Phys. Rev. Lett.* **2010**, *105*, 226102.
(9) Breckenfeld, E.; Shah, A. B.; Martin, L. W. Strain Evolution in Non-Stoichiometric Heteroepitaxial Thin-Film Perovskites. *J. Mater. Chem. C* **2013**, *1*, 8052−8059.
(10) Breckenfeld, E.; Wilson, R.; Karthik, J.; Damodaran, A. R.; Cahill, D. G.; Martin, L. W. Effect of Growth Induced (Non) Stoichiometry on the Structure, Dielectric Response, and Thermal Conductivity of $SrTiO_3$ Thin Films. *Chem. Mater.* **2012**, *24*, 331−337.
(11) Lenser, C.; Kuzmin, A.; Purans, J.; Kalinko, A.; Waser, R.; Dittmann, R. Probing the Oxygen Vacancy Distribution in Resistive

DOI: 10.1021/acs.chemmater.6b02542
Chem. Mater. 2016, 28, 5952−5961

Switching Fe-$SrTiO_3$ Metal-Insulator-Metal-Structures by Micro-X Ray Absorption Near-Edge Structure. *J. Appl. Phys.* **2012**, *111*, 076101.
(12) Wicklein, S.; Sambri, A.; Amoruso, S.; Wang, X.; Bruzzese, R.; Koehl, A.; Dittmann, R. Pulsed Laser Ablation of Complex Oxides: the Role of Congruent Ablation and Preferential Scattering for the Film Stoichiometry. *Appl. Phys. Lett.* **2012**, *101*, 131601.
(13) Droubay, T. C.; Qiao, L.; Kaspar, T. C.; Engelhard, M. H.; Shutthanandan, V.; Chambers, S. A. Nonstoichiometric Material Transfer in the Pulsed Laser Deposition of $LaAlO_3$. *Appl. Phys. Lett.* **2010**, *97*, 124105.
(14) Sambri, A.; Cristensen, D. V.; Trier, F.; Chen, Y. Z.; Amoruso, S.; Pryds, N.; Bruzzese, R.; Wang, X. Plasma Plume Effects on the Conductivity of Amorphous-$LaAlO_3$/$SrTiO_3$ Interfaces Grown by Pulsed Laser Deposition in O_2 and Ar. *Appl. Phys. Lett.* **2012**, *100*, 231605.
(15) Breckenfeld, E.; Bronn, N.; Karthik, J.; Damodaran, A. R. Effect of Growth Induced (Non) Stoichiometry on Interfacial Conductance in $LaAlO_3$/$SrTiO_3$. *Phys. Rev. Lett.* **2013**, *110*, 196804.
(16) Breckenfeld, E.; Wilson, R. B.; Martin, L. W. Effect of Growth Induced (Non)Stoichiometry on the Thermal Conductivity, Permittivity, and Dielectric Loss of $LaAlO_3$ Films. *Appl. Phys. Lett.* **2013**, *103*, 082901.
(17) Breckenfeld, E.; Bronn, N.; Mason, N.; Martin, L. W. Tunability of Conduction at the $LaAlO_3$/$SrTiO_3$ Heterointerface: Thickness and Compositional Studies. *Appl. Phys. Lett.* **2014**, *105*, 121610.
(18) Chambers, S. A.; Engelhard, M. H.; Shutthanandan, V.; Zhu, Z.; Droubay, T. C.; Qiao, L.; Sushko, P. V.; Feng, T.; Lee, H. D.; Gustafsson, T.; Garfunkel, E.; Shah, A. B.; Zuo, J. M.; Ramasse, Q. M. Instability, Intermixing and Electronic Structure at the Epitaxial LaAlO3/SrTiO3(001) Heterojunction. *Surf. Sci. Rep.* **2010**, *65*, 317−352.
(19) Qiao, L.; Zhang, K. H. L.; Bowden, M. E.; Varga, T.; Shutthanandan, V.; Colby, R.; Du, Y.; Kabius, B.; Sushko, P. V.; Biegalski, M. D.; Chambers, S. A. The Impacts of Cation Stoichiometry and Substrate Surface Quality on Nucleation, Structure, Defect Formation, and Intermixing in Complex Oxide Heteroepitaxy-$LaCrO_3$ on $SrTiO_3$ (001). *Adv. Funct. Mater.* **2013**, *23*, 2953−2963.
(20) Chen, Y. Z.; Bovet, N.; Trier, F.; Christensen, D. V.; Qu, F. M.; Andersen, N. H.; Kasama, T.; Zhang, W.; Giraud, R.; Dufouleur, J.; Jespersen, T. S.; Sun, J. R.; Smith, A.; Nygård, J.; Lu, L.; Büchner, B.; Shen, B. G.; Linderoth, S.; Pryds, N. A High-Mobility Two-Dimensional Electron Gas at the Spinel/Perovskite Interface of Γ-Al_2O_3/$SrTiO_3$. *Nat. Commun.* **2013**, *4*, 1371.
(21) Breckenfeld, E.; Chen, Z.; Damodaran, A. R.; Martin, L. W. Effects of Nonequilibrium Growth, Nonstoichiometry, and Film Orientation on the Metal-to-Insulator Transition in $NdNiO_3$ Thin Films. *ACS Appl. Mater. Interfaces* **2014**, *6*, 22436−22444.
(22) Catalan, G.; Scott, J. F. Physics and Applications of Bismuth Ferrite. *Adv. Mater.* **2009**, *21*, 2463−2485.
(23) Damodaran, A. R.; Agar, J. C.; Pandya, S.; Chen, Z.; Dedon, L.; Xu, R.; Apgar, B.; Saremi, S.; Martin, L. W. New Modalities of Strain-Control of Ferroelectric Thin Films. *J. Phys.: Condens. Matter* **2016**, *28*, 263001.
(24) Sando, D.; Barthélémy, A.; Bibes, M. BiFeO3 Epitaxial Thin Films and Devices: Past. *J. Phys.: Condens. Matter* **2014**, *26*, 473201.
(25) Basu, S. R.; Martin, L. W.; Chu, Y. H.; Gajek, M.; Ramesh, R.; Rai, R. C.; Xu, X.; Musfeldt, J. L. Photoconductivity in $BiFeO_3$ Thin Films. *Appl. Phys. Lett.* **2008**, *92*, 091905.
(26) Ihlefeld, J. F.; Podraza, N. J.; Liu, Z. K.; Rai, R. C.; Xu, X. Optical Band Gap of $BiFeO_3$ Grown by Molecular-Beam Epitaxy. *Appl. Phys. Lett.* **2008**, *92*, 142908.
(27) Kumar, A.; Rai, R. C.; Podraza, N. J.; Denev, S.; Ramirez, M.; Chu, Y.-H.; Martin, L. W.; Ihlefeld, J.; Heeg, T.; Schubert, J.; Schlom, D. G.; Orenstein, J.; Ramesh, R.; Collins, R. W.; Musfeldt, J. L.; Gopalan, V. Linear and Nonlinear Optical Properties of $BiFeO_3$. *Appl. Phys. Lett.* **2008**, *92*, 121915.
(28) Qi, X.; Dho, J.; Tomov, R.; Blamire, M. G.; MacManus-Driscoll, J. L. Greatly Reduced Leakage Current and Conduction Mechanism in Aliovalent-Ion-Doped $BiFeO_3$. *Appl. Phys. Lett.* **2005**, *86*, 062903.
(29) Kim, J. K.; Kim, S. S.; Kim, W.-J.; Bhalla, A. S.; Guo, R. Enhanced Ferroelectric Properties of Cr-Doped $BiFeO_3$ Thin Films Grown by Chemical Solution Deposition. *Appl. Phys. Lett.* **2006**, *88*, 132901.
(30) Lee, Y.-H.; Wu, J.-M.; Lai, C.-H. Influence of La Doping in Multiferroic Properties of $BiFeO_3$ Thin Films. *Appl. Phys. Lett.* **2006**, *88*, 042903.
(31) Yang, C.-H.; Kan, D.; Takeuchi, I.; Nagarajan, V.; Seidel, J. Doping $BiFeO_3$: Approaches and Enhanced Functionality. *Phys. Chem. Chem. Phys.* **2012**, *14*, 15953−15962.
(32) Lahmar, A.; Zhao, K.; Habouti, S.; Dietze, M.; Solterbeck, C. H.; Es-Souni, M. Off-Stoichiometry Effects on $BiFeO_3$ Thin Films. *Solid State Ionics* **2011**, *202*, 1−5.
(33) Yan, J.; Gomi, M.; Hattori, T.; Yokota, T.; Song, H. Effect of Excess Bi on Structure and Ferroelectric Properties of Polycrystalline $BiFeO_3$ Thin Films. *Thin Solid Films* **2013**, *542*, 150−154.
(34) Xie, X.; Yang, S.; Zhang, F.; Fan, S.; Che, Q.; Wang, C.; Guo, X.; Zhang, L. Effects of Excess Bi on Structure and Electrical Properties of $BiFeO_3$ Thin Films Deposited on Indium Tin Oxide Substrate Using Sol−Gel Method. *J. Mater. Sci.: Mater. Electron.* **2015**, *26*, 10095−10101.
(35) Karthik, J.; Damodaran, A. R.; Martin, L. W. Epitaxial Ferroelectric Heterostructures Fabricated by Selective Area Epitaxy of $SrRuO_3$ Using an MgO Mask. *Adv. Mater.* **2012**, *24*, 1610−1615.
(36) Ihlefeld, J. F.; Kumar, A.; Gopalan, V.; Schlom, D. G.; Chen, Y. B.; Pan, X. Q.; Heeg, T.; Schubert, J.; Ke, X.; Schiffer, P.; Orenstein, J.; Martin, L. W.; Chu, Y.-H.; Ramesh, R. Adsorption-Controlled Molecular-Beam Epitaxial Growth of $BiFeO_3$. *Appl. Phys. Lett.* **2007**, *91*, 071922.
(37) Gurbich, A. F. SigmaCalc Recent Development and Present Status of the Evaluated Cross-Sections for IBA. *Nucl. Instrum. Methods Phys. Res., Sect. B* **2016**, *371*, 27−32.
(38) Ziegler, J. F.; Ziegler, M. D.; Biersack, J. P. SRIM − the Stopping and Range of Ions in Matter (2010). *Nucl. Instrum. Methods Phys. Res., Sect. B* **2010**, *268*, 1818−1823.
(39) Chu, Y.-H.; He, Q.; Yang, C.-H.; Yu, P.; Martin, L. W.; Shafer, P.; Ramesh, R. Nanoscale Control of Domain Architectures in $BiFeO_3$ Thin Films. *Nano Lett.* **2009**, *9*, 1726−1730.
(40) Jang, H. W.; Ortiz, D.; Baek, S.-H.; Folkman, C. M.; Das, R. R.; Shafer, P.; Chen, Y.; Nelson, C. T.; Pan, X.; Ramesh, R.; Eom, C.-B. Domain Engineering for Enhanced Ferroelectric Properties of Epitaxial (001) $BiFeO_3$ Thin Films. *Adv. Mater.* **2009**, *21*, 817−823.
(41) Kleibeuker, J. E.; Koster, G.; Siemons, W.; Dubbink, D.; Kuiper, B.; Blok, J. L.; Yang, C.-H.; Ravichandran, J.; Ramesh, R.; ten Elshof, J. E.; Blank, D. H. A.; Rijnders, G. Atomically Defined Rare-Earth Scandate Crystal Surfaces. *Adv. Funct. Mater.* **2010**, *20*, 3490−3496.
(42) Yu, P.; Luo, W.; Yi, D.; Zhang, J.-X.; Rossell, M. D.; Yang, C. H.; You, L.; Singh-Bhalla, G.; Yang, S. Y.; He, Q.; Ramasse, Q. M.; Erni, R.; Martin, L. W.; Chu, Y.-H.; Pantelides, S. T.; Pennycook, S. J.; Ramesh, R. Interface Control of Bulk Ferroelectric Polarization. *Proc. Natl. Acad. Sci. U. S. A.* **2012**, *109*, 9710−9715.
(43) Schottky, W. Halbleitertheorie Der Sperrschicht. *Naturwissenschaften* **1938**, *26*, 843−843.
(44) Frenkel, J. On Pre-Breakdown Phenomena in Insulators and Electronic Semi-Conductors. *Phys. Rev.* **1938**, *54*, 647.
(45) Simmons, J. G. Poole-Frenkel Effect and Schottky Effect in Metal-Insulator-Metal Systems. *Phys. Rev.* **1967**, *155*, 657−660.
(46) Yeargan, J. R.; Taylor, H. L. The Poole-Frenkel Effect with Compensation Present. *J. Appl. Phys.* **1968**, *39*, 5600−5604.
(47) Mott, N. F.; Gurney, R. W. *Electronic Processes in Ionic Crystals*, 2nd ed.; Clarendon Press: Oxford, U.K., 1940.
(48) Lampert, M. A.; Mark, P. *Current Injection in Solids*; Academic Press: New York, 1970.
(49) Pabst, G. W.; Martin, L. W.; Chu, Y.-H.; Ramesh, R. Leakage Mechanisms in $BiFeO_3$ Thin Films. *Appl. Phys. Lett.* **2007**, *90*, 072902.
(50) Iakovlev, S.; Solterbeck, C. H.; Kuhnke, M.; Es-Souni, M. Multiferroic $BiFeO_3$ Thin Films Processed via Chemical Solution Deposition: Structural and Electrical Characterization. *J. Appl. Phys.* **2005**, *97*, 094901.

DOI: 10.1021/acs.chemmater.6b02542
Chem. Mater. 2016, 28, 5952−5961

(51) Blom, P.; Wolf, R.; Cillessen, J.; Krijn, M. Ferroelectric Schottky Diode. *Phys. Rev. Lett.* **1994**, *73*, 2107−2110.
(52) Lee, J. J.; Desu, S. B. The Shifting of P-E Hysteresis Loop by the Asymmetric Contacts on Ferroelectric PZT Thin Films. *Ferroelectr., Lett. Sect.* **1995**, *20*, 27−34.
(53) Agar, J. C.; Damodaran, A. R.; Velarde, G. A.; Pandya, S.; Mangalam, R. V. K.; Martin, L. W. Complex Evolution of Built-in Potential in Compositionally-Graded $PbZr_{1-x}Ti_xO_3$ Thin Films. *ACS Nano* **2015**, *9*, 7332−7342.
(54) Palkar, V. R.; John, J.; Pinto, R. Observation of Saturated Polarization and Dielectric Anomaly in Magnetoelectric $BiFeO_3$ Thin Films. *Appl. Phys. Lett.* **2002**, *80*, 1628−1630.

DOI: 10.1021/acs.chemmater.6b02542
Chem. Mater. 2016, 28, 5952−5961